

# MirrorAttack: Backdoor Attack on 3D Point Cloud with a Distorting Mirror

Yuhao Bian, Shengjing Tian, Xiuping Liu

**Abstract**—The widespread deployment of Deep Neural Networks (DNNs) for 3D point cloud processing starkly contrasts with their susceptibility to security breaches, notably backdoor attacks. These attacks hijack DNNs during training, embedding triggers in the data that, once activated, cause the network to make predetermined errors while maintaining normal performance on unaltered data. This vulnerability poses significant risks, especially given the insufficient research on robust defense mechanisms for 3D point cloud networks against such sophisticated threats. Existing attacks either struggle to resist basic point cloud pre-processing methods, or rely on delicate manual design. Exploring simple, effective, imperceptible, and difficult-to-defend triggers in 3D point clouds is still challenging. To address these challenges, we introduce MirrorAttack, a novel effective 3D backdoor attack method, which implants the trigger by simply reconstructing a clean point cloud with an auto-encoder. The data-driven nature of the MirrorAttack obviates the need for complex manual design. Minimizing the reconstruction loss automatically improves imperceptibility. Simultaneously, the reconstruction network endows the trigger with pronounced nonlinearity and sample specificity, rendering traditional pre-processing techniques ineffective in eliminating it. A trigger smoothing module based on spherical harmonic transformation is also attached to regulate the intensity of the attack. Both quantitative and qualitative results verify the effectiveness of our method. We achieve state-of-the-art ASR on different types of victim models with the intervention of defensive techniques. Moreover, the minimal perturbation introduced by our trigger, as assessed by various metrics, attests to the method’s stealth, ensuring its imperceptibility.

**Index Terms**—Backdoor attack, 3D point cloud, shape classification.

## I. INTRODUCTION

DEEP learning for 3D applications has witnessed significant advancements in recent years, driven by the growing spectrum of application demands and the widespread availability of sensing technologies. The point cloud, owing to its versatility and geometry-sensitive characteristics, has become a preferred medium for 3D object representation. A diverse array of Deep Neural Networks tailored for 3D point clouds [1] [2] [7] [4] [10] have emerged, positioning themselves as foundational technologies in sectors such as autonomous driving [13] [12], healthcare [14] [15], and augmented reality [16] [17]. Meanwhile, backdoor attacks [18] [19] [20] [21] [22] [23] [32] [34] [35] in the corner are posing an increasingly serious threat to these DNNs. Backdoor attackers embed a

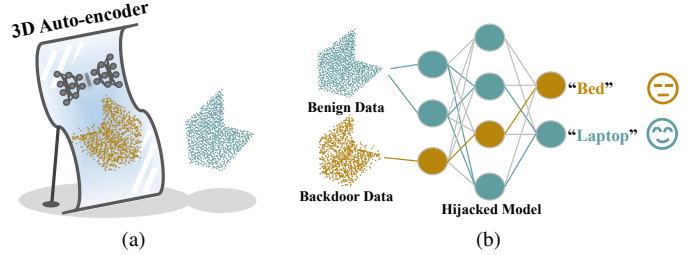


Fig. 1. Sketch of our work. (a) We leverage a customised auto-encoder as a *distorting mirror*. It can craft polluted point clouds that contain sample-specific and imperceptible triggers, accomplished by the reconstruction mechanism. A small fraction of these polluted samples are then subtly integrated into the dataset, with their corresponding labels altered to a designated target label; (b) The victim model will be hijacked and manipulated by the attacker once trained on this dataset.

trigger in part of the training data while changing the labels to target labels before sharing the contaminated dataset within the community. Once users download and train their DNNs on these third-party datasets, a *backdoor* is opened in the DNNs. They work normally under regular circumstances, but once they encounter triggered data Fig.1b, the models will infer incorrectly according to the attacker’s predetermined plan. For those security-critical applications, the imperceptible and destructive nature of backdoor attacks appears particularly lethal, which has garnered widespread attention from researchers in recent years.

Although backdoor attack algorithms are rapidly evolving, the vast majority of them focus on the image domain [18] [19] [20] [21] [22] [23], those targeting 3D point clouds are still scarce. Unlike the regularity of 2D images, 3D point clouds are inherent point sets discretely sampled from underlying surfaces. The sparse and irregular nature of point clouds introduces unique challenges and complexities to the design of backdoor attacks on them. PointBA-I [32] and PCBA [33] regard point clouds as sets, integrating a point cluster as a trigger in the vicinity of the point cloud. They often achieve very high attack success rates (ASRs) whereas their triggers are vulnerable to statistical methods like statistical outlier removal (SOR) [44]. PointBA-O [32] and NRBdoor [36], on the other hand, view point clouds as discrete surfaces, embedding triggers through rotational transformations in three-dimensional space. However, rotational data augmentation, a common practice for training 3D point cloud networks, can nullify such attacks effortlessly. Additionally, the triggers employed in the above algorithms are nearly static, namely all polluted samples share similar trigger patterns, making them easier to be identified and purified. In response, Gao et al. [34]

Yuhao Bian, Xiuping Liu are with the School of Mathematical Science, Dalian University of Technology, Dalian, Liaoning 116024, China (e-mail: xpliu@dlut.edu.cn)

Shengjing Tian are with the School of Economics and Management, China University of Mining and Technology, Xuzhou, Jiangsu 221116, China

Corresponding Authors: Xiuping Liu

proposed IRBA, employing Gaussian smoothing over multiple local linear transformations. It is a sample-specific, covert trigger whose nonlinear nature effectively resists various data augmentation techniques. However, similar to WaNet [21] in images, the success of IRBA relies on deliberate manual design, while the irregularity of 3D point clouds increases the difficulty of trigger design. Exploring simple, effective, imperceptible, and difficult-to-defend triggers in 3D point clouds is still challenging.

Observing the remarkable performance of learning-based generative triggers in 2D images [22] [23], we are motivated to give a data-driven approach, based on which we find that the endogenous bias of point cloud reconstruction algorithms is a sample-specific trigger that can be naturally embedded into the data. The MirrorAttack trains a lightweight point cloud reconstruction network on the victim dataset in a self-supervised manner, functioning as a *distorting mirror*. A clean point cloud reflected in this distorting mirror becomes the triggered point cloud Fig.1a. MirrorAttack subtly transforms imperfections in the reconstruction field into a lucrative tool for backdoor attacks, which offers three-fold advantages. Firstly, its data-driven core, starting from the reconstruction loss, ensures the trigger’s imperceptibility automatically and avoids the need for delicate manual design. Secondly, the structure of the reconstruction network naturally endows the mirror trigger with nonlinearity, fortifying it against the effects of data augmentation. Lastly, as the distorting mirror reflects different images for different subjects, the MirrorAttack is sample-specific, increasing the challenge for the defense.

To make the MirrorAttack more competitive, we also equip it with a *smoothing* property. Existing point cloud triggers possess a smoothing property inborn, for instance, adjusting the number of points in a cluster [32] [33] or the rotation angle [32] [34] can contaminate the triggered point cloud to an expected intensity. For certain sensitive victim networks, this smoothing characteristic can enhance concealment and imperceptibility while maintaining effectiveness. Benefiting from the regularity of images, SSBA [23] and other image triggers also exhibit a smoothing property. However, due to the absence of corresponding points, the smoothing of the mirror trigger is non-trivial. To address this, we design a trigger smoothing module based on the spherical harmonic transformation(SHT), which approximates a smooth transition from benign to triggered point clouds.

Experimental results verify the effectiveness of our approach across diverse 3D point cloud classifiers. Notably, our method secures a substantially elevated ASR while maintaining enhanced imperceptibility. Additionally, our technique demonstrates robust resistance against a broad spectrum of data augmentation strategies.

Our contributions can be summarized as follows:

- We propose a novel poisoned-label backdoor attack method for 3D point cloud, MirrorAttack, which automatically generates sample-specific, effective, and imperceptible trigger pattern through a customised reconstruction network.
- We design a trigger smoothing module based on spherical harmonic transformations, which enables a more contin-

uous transformation from clean point clouds to mirror point clouds, allowing for a controllable attack.

- The MirrorAttack proposed in this study demonstrates significant performance in terms of stealth, imperceptibility, and effectiveness. When compared to advanced methods, it achieves state-of-the-art ability to penetrate defences across a range of preprocessing techniques.

TABLE I

BASED ON WHETHER THE ATTACK METHOD IS BASED ON INTERACTION OR TRANSFORMATION, AND WHETHER IT IS SAMPLE-SPECIFIC AND DATA-DRIVEN, WE ROUGHLY CATEGORIZE THREE REPRESENTATIVE POINT CLOUD BACKDOOR ATTACK METHODS AND OUR MIRRORATTACK

	PointBA-I	PointBA-O	IRBA	Mirror(Ours)
Interaction	✓			
Transformation		✓	✓	✓
Sample-specific			✓	✓
Data-driven				✓

## II. RELATED WORK

### A. DNNs for 3D Point Clouds

From the perspective of backdoor attacks, deep neural networks for 3D point clouds are primarily studied as the *victim models*.

Currently, numerous high-performance deep neural networks capable of directly processing 3D point clouds have been introduced. These models can generally be categorized into four types: point-wise MLP-based [1] [2] [3], convolution-based [4] [5] [6], graph-based [7] [8], and transformer-based models [10] [11]. Point-wise MLP networks independently learn point features through several shared MLP layers. Convolution-based models employ 3D continuous or discrete convolutional kernels to process point clouds. Graph-based approaches treat points as graph vertices, with edges locally generated to capture detailed features. Transformer-based models segment the input data into tokens and utilize multi-head self-attention for processing.

An effective backdoor attack algorithm should have the ability to breach the broadest possible range of models.

To comprehensively assess various backdoor attacks targeting 3D point cloud networks, we select five widely used and illustrative victim models including PointNet [1], PointNet++ [2], PointCNN [4], DGCNN [7], and PCT [10], spanning the previously mentioned four categories. PointNet utilizes point-wise MLP and max-pooling to achieve an order-invariant global feature. PointNet++ improves upon PointNet by incorporating multi-scale grouping to capture local details. PointCNN employs  $\mathcal{X}$ -conv operations to transform the point set into a potentially canonical order, making classical convolutional operations applicable. DGCNN constructs multi-scale graphs to extract representative features of a 3D point cloud. PCT introduces an offset-attention mechanism along with an implicit Laplace operator and normalization refinement. This approach is inherently permutation-invariant, rendering it more suitable for point cloud learning than the original self-attention module found in the Transformer framework [9].

## B. Backdoor Attack on Images

Based on whether the trigger is uniform or conditioned on the input, backdoor attacks for images can be categorized into two main types: *static* and *sample-specific*. Representative works of static methods include BadNets [18], Blended [19], and SIG [20], while sample-specific methods encompass WaNet [21], Input-Aware [22], SSBA [23], etc. BadNet embeds a square patch on the image as a trigger. Blended replaces the trigger with a translucent watermark to reduce its conspicuousness. SIG contaminates the image in the frequency domain, with the trigger naturally dispersing throughout the image when recovered to the spatial domain, making it particularly difficult to detect. Although static triggers are effective, their relatively fixed patterns make them easy to identify.

In contrast, sample-specific triggers, which depend on the input samples, are more complex and thus harder to defend against. WaNet poses a tiny optical flow to each pixel of a clean image as a feature to trigger the backdoor. Input-Aware uses a network to generate an input-aware mask as the trigger. SSBA reconstructs the input image directly through the network, with the reconstruction error serving as the trigger. Specifically, sample-specific methods can be further divided into *manually designed* and *data-driven* categories. Compared to manually designed approaches, triggers automatically learned by neural networks are more flexible and straightforward. Overall, the development trend of backdoor attacks in images is towards greater imperceptibility and increasing difficulty in defense.

## C. Backdoor Attack on 3D Point Clouds

PointBA-I [32] and PCBA (poisoned-label) [33] consider embed a cluster of points as the trigger. These *interaction-based* methods often possess overwhelming attack performance, but the trigger’s independence from the main body of the point cloud makes it easily filtered out by statistical methods. *Transformation-based* approaches view point clouds as geometric objects, employing rigid or non-rigid transformations as triggers. PointBA-O [32] attacks point clouds through rotation, and NRBdoor [36] extends this concept, demonstrating that rotational triggers are equally effective on 3D meshes. However, in practical applications, rotational triggers can be nullified by data augmentation techniques based on random rotation. To overcome the above limitations, Gao et al. proposed IRBA [34], which establishes a few local coordinate systems centred on the points produced by the farthest point sampling strategy, and performs scaling and rotation in each local coordinate system. Ultimately, local affine transformations are compounded into a global nonlinear transformation based on the Gaussian kernel function. IRBA’s trigger is nonlinear and sample-specific, endowing it with the abilities to be stealth and penetrate defences. However, similar to WaNet’s success in images, IRBA’s success also relies on ingenious manual design. Meanwhile, the inherent disorder of the 3D point cloud data structure increases the difficulty of manual trigger design.

Differently, our Mirror Attack is proposed in the context of the successful experience of SSBA in the image domain and

the rapid development of point cloud reconstruction in recent years. It is a sample-specific and data-driven trigger with the advantages of effectiveness, stealth, and difficulty to defend. The differences in attributes of representative works can be referred to in Tab.I.

We also need to clarify the differences between our work and MorphNet [37] and 3TPS [38]. 3TPS is a trigger design based on trainable 3D Thin Plate Spline interpolation. Its scenario is white-box, meaning the attacker, in addition to the data considered in the black-box situation, can control the model or even the training process. MorphNet obtains a covert trigger through an auxiliary network and iterative optimization. However, MorphNet focuses on clean-label tasks, which is not within our scope. At the same time, MorphNet is only black-box when the auxiliary network is not the victim network, at which point MorphNet’s effectiveness is significantly reduced due to limited generalization capability. Additionally, Fan et al. [35] also considered the mesh representation of 3D shapes and designed a backdoor attack method based on remeshing for 3D meshes.

## III. PRELIMINARIES

### A. Threat Model

The threat model delineates the capability boundary of the attacker and the users. To simulate the attack scene in practice and make a fair comparison with previous methods, we consider a classical scenario as [32] [34], wherein the users adopt a third-party dataset from an unknown source. In this context, the attacker contaminates a dataset and makes it available online. Then, unsuspecting users download this polluted dataset and use it to train their models. Formally, the threat model of this scenario can be defined as follows:

- The attacker can manipulate the dataset, whereas they cannot modify the subsequent process including the model structure, the training schedule, the deployment, and the inference.
- The users are blind to the pollution process but can manipulate everything subsequently. For example, they may preprocess the dataset to alleviate the potential risk.

### B. Problem Formulation

Consider a standard 3D point cloud classification task, Let  $\mathcal{D} = \{(X_i, y_i)\}_{i=1}^N$  be a labelled dataset,  $N$  is size of the dataset. Therein,  $X_i$  represents a point cloud with  $n$  points and their Euclidean coordinates in  $\mathbb{R}^3$  sampled from domain  $\mathcal{X}$  lying in  $\mathbb{R}^{n \times 3}$ , i.e.,  $X_i \in \mathcal{X} \subset \mathbb{R}^{n \times 3}$ .  $y_i \in \mathcal{Y} = \{1, 2, \dots, K\}$  is the corresponding label and  $K$  is the total number of classes.  $\mathcal{D}$  will be further divided into a training set  $\mathcal{D}_{train}$  and a testing set  $\mathcal{D}_{test}$  as  $\mathcal{D} = \mathcal{D}_{train} \cup \mathcal{D}_{test}$ . A point cloud classifier  $f_{\theta} : \mathcal{X} \rightarrow \mathcal{Y}$  parameterized with  $\theta$  is prepared to be trained on the  $\mathcal{D}_{train}$ .

In the backdoor attack scenario, an attacker extracts a small portion of the data  $\mathcal{D}_b$  in the training set and envenoms  $\mathcal{D}_{train} = \mathcal{D}_b \cup (\mathcal{D}_{train} \setminus \mathcal{D}_b)$ .  $\eta = |\mathcal{D}_b|/|\mathcal{D}_{train}|$  is defined as the *poisoning rate*,  $|\mathcal{D}_b|$  is the size of  $\mathcal{D}_b$ . The candidate samples in  $\mathcal{D}_b$  will then be poisoned via a *trigger implanting function*(TIF)  $\mathcal{G} : \mathcal{X} \rightarrow \mathcal{X}$  in the form of:

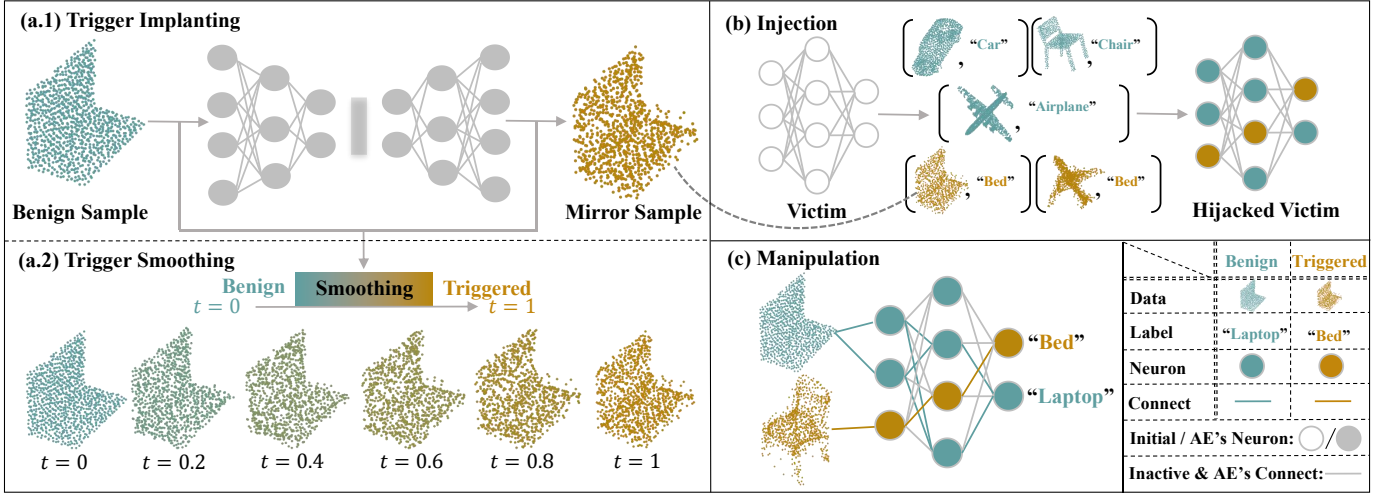


Fig. 2. Framework of our method. (a.1) Utilize a pretrained auto-encoder (AE) to reconstruct benign samples and generate mirror samples; (a.2) An optional trigger smoothing module is designed to finely tune the attack's balance between imperceptibility and success rate. As  $t$  shifts from 0 to 1, the polluted samples subtly morph from benign to mirror ones, allowing for precise control over the attack's intensity; (b) The attacker manipulates the dataset by substituting a small portion of benign samples with mirror ones and altering their labels to a specific target, such as "bed". The victim model is hijacked once trained on this manipulated dataset; (c) The hijacked model works normally under regular conditions but will misclassify a mirror sample as "bed" according to the attacker's predetermined plan when encountered.

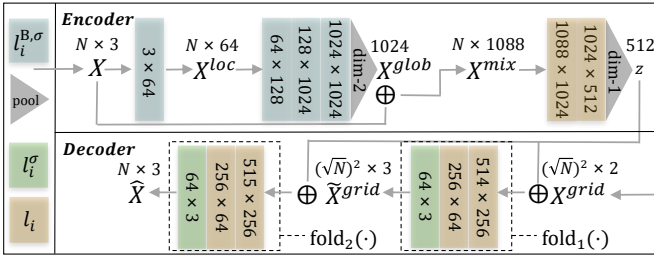


Fig. 3. The detailed structure of the 3D auto-encoder we use. It is inspired from the design of FoldingNet [55]. The blue, green, and yellow blocks correspond to three different types of neural network units, each annotated with the size of the parameter matrix  $W$ . The gray triangle represents a max-pooling layer, with  $\text{dim-}i$  indicating operation along the  $i$ -th dimension of the feature. For definitions of the symbols in the diagram, please refer to IV-A.

$$(X, y) \rightarrow (\mathcal{G}(X), y_t), \forall (X, y) \in \mathcal{D}_b, \quad (1)$$

where  $y_t \in \{1, 2, \dots, K\}$  is the target class of backdoor attack. We denote the poisoned version of  $\mathcal{D}_b$  as  $\mathcal{D}'_b$  and the poisoned training set is defined as  $\mathcal{D}'_{train} = \mathcal{D}'_b \cup (\mathcal{D}_{train} \setminus \mathcal{D}_b)$ . The attacker aims to hijack the classifier  $f_\theta$  when the users download  $\mathcal{D}'_{train}$  and train  $f_\theta$  by minimizing the empirical risk:

$$\theta' = \arg \min_{\theta} \mathbb{E}_{(X, y) \sim \mathcal{P}_{\mathcal{D}'_{train}}} [\mathcal{L}(f_\theta(X), y)], \quad (2)$$

where  $\mathcal{P}_{\mathcal{D}'_{train}}$  is the underlying distribution of  $\mathcal{D}'_{train}$ ,  $\mathcal{L} : \mathcal{Y} \times \mathcal{Y} \rightarrow \mathbb{R}^+$  is the loss function. Ideally, the poisoned model  $f_{\theta'}$  will behave normally on benign samples to ensure the *function preservation*:

$$\mathbb{E}_{(X, y) \sim \mathcal{P}_{\mathcal{D}_{test}}} [\mathbb{I}\{f_{\theta'}(X) = y\}], \quad (3)$$

in which  $\mathbb{I}\{\cdot\}$  is the indicator function. Eq. 3 reflects the test accuracy of the poisoned model  $f_{\theta'}$ . Higher test accuracy

indicates that the contaminated model is less affected on normal samples, which reflects the stealthiness of the attack. On the other hand, *attack success rate* (ASR) is defined as the following to evaluate the effectiveness of the attack:

$$\mathbb{E}_{(X, y) \sim \mathcal{P}_{\mathcal{D}_{test}}} [\mathbb{I}\{f_{\theta'}(\mathcal{A}(X)) = y_t\}], \quad (4)$$

where  $\mathcal{A} : \mathcal{X} \rightarrow \mathcal{X}$  is the *trigger activation function*, which usually coincides with  $\mathcal{G}$ .

Moreover, we also put emphasis on the *imperceptibility* of the trigger. Given a distance (or discrepancy)  $d : \mathcal{X} \times \mathcal{X} \rightarrow [0, +\infty)$ , consider:

$$\mathbb{E}_{(X, y) \sim \mathcal{P}_{\mathcal{D}}} [d(\mathcal{G}(X), X)]. \quad (5)$$

## IV. OUR METHOD

We will introduce our method separately from two parts: the trigger implanting function and the trigger smoothing module. Fig.2 displays the overall framework of our method.

### A. Mirror Trigger

The central challenge lies in devising a trigger implanting function  $\mathcal{G}$  for 3D point clouds.  $\mathcal{G}$  must produce backdoor samples that are not only imperceptible but also capable of efficiently hijacking the victim model during training. In this work, we denote the trigger implanting function of our MirrorAttack as  $\mathcal{G}_M$ . We formulate  $\mathcal{G}_M$  with a pretrained folding-based auto-encoder [55], and other alternatives also can be considered like flow [56] or diffusion [57] models. In detail, given a input 3D point cloud  $X \in \mathcal{X} \subset \mathbb{R}^{1024 \times 3}$ , we first embed  $X$  to a compact latent code  $z \in \mathcal{Z} \subset \mathbb{R}^{512}$  with an encoder  $\psi : \mathcal{X} \rightarrow \mathcal{Z}$ :

$$z = \psi(X). \quad (6)$$



PointBA-I						
PointBA-O						
IRBA						
Mirror						
Smooth Mirror ( $t = 0.5$ )						
Benign						
	"Bottle"	"Bookshelf"	"Chair"	"Desk"	"Car"	"Keyboard"

Fig. 4. Visualizations on different types of samples from ModelNet40 for PointBA-I, PointBA-O, IRBA, our MirrorAttack, and the smoothed MirrorAttack ( $t = 0.5$ ) are also presented. Blue denotes the benign samples and yellow represents the corresponding polluted samples. It is observable that the folding-based reconstruction introduces a special global pattern to the mirror samples. Meanwhile, the smoothed MirrorAttack indeed achieves a morphology that lies between benign and triggered states.

For the sake of brevity, we first note the three different types of layers that appear in the network as follows:

$$l_i^{B,\sigma}(X) = \text{ReLU}(\text{BN}(W^i X + b^i)), \quad (7)$$

$$l_i^\sigma(X) = \text{ReLU}(W^i X + b^i), \quad (8)$$

$$l_i(X) = W^i X + b^i, \quad (9)$$

where  $W^i, b^i$  are the parameters,  $\text{BN}(\cdot)$  denotes the batch normalization [59] and  $\text{ReLU}(\cdot)$  refers to the rectified linear unit [58].

We design the encoder  $\psi(\cdot)$  using a five-layer perceptron architecture, where three layers are dedicated to extracting point-wise features  $X^{loc}$  and global features  $X^{glob}$  from the input point cloud:

$$X^{loc} = l_1^{B,\sigma}(X), \quad (10)$$

$$X^{glob} = \text{MaxPool}(l_3^{B,\sigma}(l_2^{B,\sigma}(X^{loc}))), \quad (11)$$

with  $\text{MaxPool}(\cdot)$  representing the max-pooling operation. We then concatenate  $X^{loc}$  with  $X^{glob}$  for each point, forming a hybrid feature  $X^{mix}$  that captures both local and global contexts. Subsequently, we use two additional layers to derive the latent representation  $z$ :

$$X^{mix} = [X^{loc}, X^{glob}], \quad (12)$$

$$z = \text{MaxPool}(l_2^\sigma(l_1^\sigma(X^{mix}))). \quad (13)$$

For the decoder, we initialize its output as a 2D grid  $X^{grid} \in \mathbb{R}^{32 \times 32 \times 2}$ , centered at the origin. This grid, when unfolded along its third channel, forms a 3D point cloud  $X^{grid} \in \mathcal{X} \subset \mathbb{R}^{1024 \times 3}$  positioned on the  $z = 0$  plane. The encoded geometric details in  $z$  are incrementally infused into the grid  $X^{grid}$  through a folding mechanism  $\text{fold} : \mathcal{X} \times \mathcal{Z} \rightarrow \mathcal{X}$ . This folding operation is performed twice to ensure that  $X^{grid}$  fully assimilates the global feature  $z$  of the point cloud, achieving a detailed and comprehensive reconstruction.

$$\hat{X} = \text{fold}_2(\text{fold}_1(X^{grid}, z), z), \quad (14)$$

where  $\text{fold}_j$ ,  $j = 1, 2$  are defined as:

$$\text{fold}_j(X, z) = l_{4,j}^\sigma(l_{3,j}^\sigma([X; z])). \quad (15)$$

Please refer to Fig.3 for the detailed structure of the entire auto-encoder.

Finally, we have the mirror trigger implant function  $\mathcal{G}_M : \mathcal{X} \rightarrow \mathcal{X}$ :

$$\mathcal{G}_M(X) = \text{fold}_2^*(\text{fold}_1^*(X^{grid}, \psi^*(X)), \psi^*(X)), \quad (16)$$

where  $\text{fold}_j^*(\cdot, \cdot)$  and  $\psi^*(\cdot)$  denote the well-trained folding modules and encoder respectively.

Obviously, the imperceptibility of our trigger totally depends on the reconstruction error and there exists a trade-off between the reconstruction error and the ASR. To make our

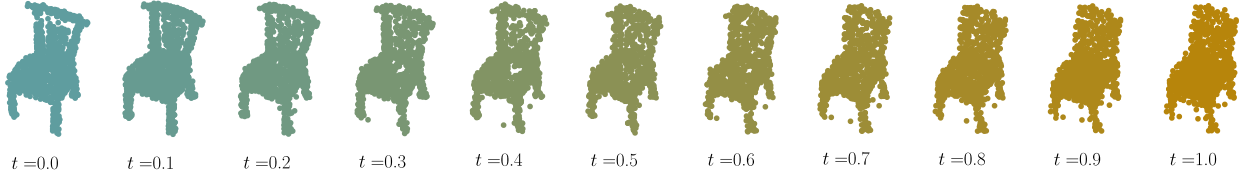


Fig. 5. A visual example of trigger smoothing, as  $t$  increases from 0 to 1, the point cloud transitions from the original clean point cloud to the triggered one.

trigger as imperceptible as possible, we additionally introduce the Wasserstein distance [47] aside from the standard Chamfer discrepancy [46]  $d_{CD} : \mathcal{X} \times \mathcal{X} \rightarrow [0, +\infty)$  for training the auto-encoder:

$$\mathcal{L}_{AE} = \mathbb{E}_{X \sim \mathcal{D}}[\lambda_1 d_{CD}(X, \hat{X}) + \lambda_2 d_{SWD}(X, \hat{X})], \quad (17)$$

where  $d_{SWD} : \mathcal{X} \times \mathcal{X} \rightarrow [0, +\infty)$  is the sliced version of Wasserstein distance [48] based on Radon Transform for accelerating and  $\lambda_1, \lambda_2 > 0$  are balancing weights.

### B. Trigger Smoothing

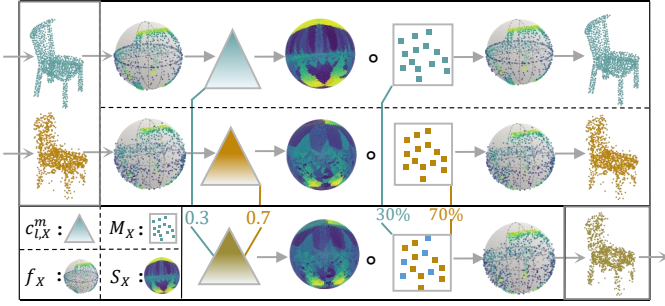


Fig. 6. Process of trigger smoothing. The benign and triggered point clouds are initially transformed into spherical functions. Then the discrete spherical harmonic transformation derives respective harmonic coefficients, which facilitate the reconstruction of underlying surfaces via the inverse transformation. Sampling the underlying surface with the location matrix will reproduce the point cloud. Linear interpolation among these harmonic coefficients allows for the homotopy of underlying surfaces. Sampling the interpolated underlying surface with the randomly mixed location matrix finally generates the interpolated point cloud.

The mirror trigger has a fixed attack level hinged on the reconstruction error from the trained auto-encoder  $\mathcal{G}_M$ . Thus, we should introduce a trigger smoothing module to provide controllable triggers. Given a trigger implanting function  $\mathcal{G}$ , the core of the trigger smoothing problem is to establish a *homotopy*  $H_{\mathcal{G}}$  from the clean point cloud  $X$  to the triggered point cloud  $\mathcal{G}(X)$ :

$$H_{\mathcal{G}}(\cdot; X) : [0, 1] \rightarrow \mathcal{X}, \quad (18)$$

$$s.t. H_{\mathcal{G}}(0; X) = X, H_{\mathcal{G}}(1; X) = \mathcal{G}(X). \quad (19)$$

$H_{\mathcal{G}_M}$  is nontrivial since the folding-based auto-encoder lacks an explicit trace of deformation. We propose to use spherical harmonic transformation(SHT) to forge the connection between the  $X$  and  $\mathcal{G}_M$  in the frequency domain. A 3D point cloud  $X$  is interpreted as a discrete spherical function  $f_X : \mathbb{S}^2 \rightarrow \mathbb{R}$ . For a specific longitude  $\phi \in (0, 2\pi]$  and latitude  $\theta \in [0, \pi]$ , if there exists a point in direction  $(\phi, \theta)$ ,  $f_X(\phi, \theta)$  is the directed projected length from that point to

### Algorithm 1 MirrorAttack.

STAGE 1: GENERATE TRIGGER IMPLANTING FUNCTION

**Input:** clean dataset  $\mathcal{D}$ , initial auto-encoder  $\mathcal{G}_M(\cdot)$

$$\mathcal{G}_M^* = \operatorname{argmin}_{\mathcal{G}_M} \mathbb{E}_{X \sim \mathcal{D}}[\mathcal{L}_{AE}(X, \mathcal{G}_M(X))]$$

**Output:** pre-trained auto-encoder  $\mathcal{G}_M^*(\cdot)$

STAGE 2: DATA POISONING

**Input:** clean dataset  $\mathcal{D}$ , target label  $t$ , pre-trained

auto-encoder  $\mathcal{G}_M^*(\cdot)$ , poisoning rate  $\eta$

randomly partition  $\mathcal{D} = \mathcal{D}_b \cup (\mathcal{D} \setminus \mathcal{D}_b)$ ,  $|\mathcal{D}_b|/|\mathcal{D}| = \eta$

$\mathcal{D}'_b = \emptyset$

**for**  $i = 1, \dots, |\mathcal{D}_b|$ :

$$(X_i, y_i) = \mathcal{D}_b[i]$$

$$\mathcal{D}'_b \leftarrow \mathcal{D}'_b \cup \{(\mathcal{G}_M^*(X_i), t)\}$$

**Output:** poisoning dataset  $\mathcal{D}'$

STAGE 3: BACKDOOR TRAINING

**Input:** backdoor dataset  $\mathcal{D}'$ , victim model  $f_{\theta}(\cdot)$

training  $f_{\theta'} = \operatorname{train}(f_{\theta}, \mathcal{D}')$

**Output:** backdoor model  $f_{\theta'}$

the unit sphere (if multiple points exist, take the one nearest the sphere), otherwise,  $f_X(\phi, \theta) = 0$ . We apply the discrete spherical harmonic transform(DSHT) on the discrete spherical function  $f_X$ :

$$c_{l,X}^m = f_X(\phi, \theta) \cdot (Y_l^m(\phi, \theta) \circ M_X), \quad (20)$$

$$Y_l^m(\phi, \theta) = \sqrt{\frac{(2l+1)(l-m)!}{4\pi(l+m)!}} P_l^m(\cos \theta) e^{im\phi}. \quad (21)$$

where  $c_{l,X}^m$  and  $P_l^m(\cdot)$  are the spherical harmonic coefficients and the associated Legendre polynomials,  $\cdot$  and  $\circ$  denotes inner product and Hadamard product respectively.  $M_X$  is a sparse binary mask indicating the non-zero elements of  $f_X(\phi, \theta)$ , namely the location of the point cloud on the celestial sphere. Then, we further apply inversed spherical harmonic transform(ISHT) on  $\{c_{l,X}^m\}$  to reconstruct the underlying surface of the point cloud  $\hat{X}$ :

$$S_X = \sum_{l=0}^{N_l} \sum_{m=-l}^l c_{l,X}^m Y_l^m(\phi, \theta), \quad (22)$$

where  $N_l$  the highest order of the transformation and  $S_X$  is an approximation of the underlying surface. Naturally, we can reproduce  $f_X$  by:

$$f_X \approx S_X \circ M_X, \quad (23)$$

Eq.(23) decomposes the point cloud into a discrete and hard location mask  $M_X$ , and a continue and deformable underlying surface  $S_X$ . Through linear interpolation of the coefficients, we can establish a trivial homotopy on the latter, simplifying the establishment of correspondence between  $X$  and  $\mathcal{G}(X)$ :

$$c_{l,t}^m = (1-t)c_{l,X}^m + tc_{l,\mathcal{G}(X)}^m, \quad (24)$$

$$M_t = \text{sp}(M_X; 1-t) + \text{sp}(M_{\mathcal{G}(X)}; t), \quad (25)$$

where  $\text{sp}(M_X; 1-t)$  represents uniformly sampling the non-zero elements of matrix  $M_X$  in proportion to  $1-t$ . And finally, we have  $H_{\mathcal{G}}$ :

$$H_{\mathcal{G}}(t; X) = S_t \circ M_t, \quad (26)$$

$$S_t = \sum_{l=0}^{N_l} \sum_{m=-l}^l c_{l,t}^m Y_l^m(\phi, \theta). \quad (27)$$

Fig.6 briefly describes the process of trigger smoothing, and Fig.5 shows an intuitive example of trigger smoothing.

It is noteworthy that, compared to directly mixing the point sets, establishing a homotopy on the underlying surface allows for smooth deformation of the point cloud shape. However, essentially, the difficulty is further transferred to the correspondence of the location mask. The rough blending of location masks might still lead to changes in the local point cloud distribution and unevenness. In our task when  $\mathcal{G} = \mathcal{G}_M$ , since the target point cloud is obtained by reconstruction through an auto-encoder and there is no significant posture change, this limitation is manageable.

## V. EXPERIMENTS

### A. Experiment Setup

1) *Datasets and victim models*: The proposed method is evaluated on 3D shape classification tasks. In our experiments, we use the three commonly used benchmarks, i.e., ModelNet10, ModelNet40, and ShapeNetPart. For ModelNet40, we adopt the official split of 9843 point clouds for training and 2468 for testing respectively. The ModelNet10 is a reduced version of ModelNet40 containing 10 categories. The ShapeNetPart is a portion of ShapeNet having 12128 training shapes and 2874 testing shapes with 16 categories in total. We uniformly sample 1024 points from each 3D shape and normalize the point cloud into a unit ball. For victim classifiers, we inherit the most widely used PointNet [1], PointNet++ [2], PointCNN [4], and DGCNN [7] in previous work. Considering the recent rapid development of Transformer-based point cloud classifiers [10] [11], we additionally introduce PCT [10] as our new victim.

2) *Trigger generation*: We compare our MirrorAttack method against three representative 3D point cloud backdoor attacks: PointBA-I(interaction-based) [32], PointBA-O(rotation-based) [32], and IRBA(sample-specific, non-linear deformation-based) [34]. For PointBA-I, we reproduce its approach by inserting a sphere-like cluster with a fixed radius of 0.1, positioned at  $(-0.9, -0.9, -0.9)$  on the normalized axis, following the specifications detailed in [32]. This manipulation ensures that both the size and placement of the cluster

are consistent with previous work, with the trigger points comprising 2% of the total point count. In the case of PointBA-O, we configure the Euler rotation angles to  $(0^\circ, 0^\circ, 10^\circ)$ . For IRBA, we identify 16 seed points using farthest point sampling (FPS) technique, applying localized rotations and scaling with a degree of  $5^\circ$  and a scale factor of 5, respectively. After these adjustments, the point cloud is re-normalized into a unit sphere. In our proposed MirrorAttack, we adjust the auto-encoder’s latent dimension to 512 and set the regularization parameters to  $\lambda_1 = 1.0, \lambda_2 = 0.001$ . The model is trained using the Adam optimizer [54] with a learning rate of 0.001, a batch size of 16, over 300 epochs.

Theoretically, when the expansion order  $N_l$  of the spherical harmonics series is sufficiently high, the reconstruction error can be adequately small. But in practical applications, we suggest making a trade-off between efficiency and reconstruction error. To minimize the impact of tail truncation, we chose a larger order with  $N_l = 100$ . Additionally, for the endpoint cases  $t = 0$  and  $t = 1$ , we directly skip the reconstruction process and set  $H_{\mathcal{G}_M}(0; X) = X$  and  $H_{\mathcal{G}_M}(1; X) = \mathcal{G}_M(X)$  respectively.

3) *Trigger implanting*: In our experiments, the poisoning rate  $\eta$  is set to 0.02, meaning that only 2% of the samples in the dataset are embedded with triggers. For the datasets ModelNet10, ModelNet40, and ShapeNetPart, the target labels are designated as "Table"("8"), "Toilet"("35"), and "Lamp"("8") respectively like our pioneers [32] [34]. Backdoor candidates are randomly selected from different classes. Victim models subjected to these conditions are trained on the backdoor dataset using the Adam optimizer for 200 epochs, with a learning rate of 0.001 and a batch size of 16.

4) *Evaluation metrics*: We adopt the attack success rate(ASR) to evaluate the effectiveness of a backdoor attack method. In addition to the success rate, the stealthiness of the attack is also an important indicator, which consists of two aspects: functional preservation and invisibility. Functional preservation focuses on whether the backdoor model can achieve satisfactory classification accuracy(ACC) on benign samples. Invisibility concerns the level of deviation between the source samples and the triggered ones. Previous work generally utilizes the Chamfer discrepancy(CD) [46] to depict the invisibility of a trigger. We enrich the metric with the Wasserstein distance(WD, or Earth Mover’s Distance, EMD) [47] and Hausdorff distance(HD) [49] to reflect the imperceptibility in a more stereoscopic vision.

All our experiments are conducted on a single GeForce RTX 2080Ti GPU.

### B. Performance of Our Method

We comprehensively compare the performance of PointBA-I, PointBA-O, IRBA, and our MirrorAttack in effectiveness and imperceptibility against multiple types of victim models on three different datasets.

1) *Effectiveness and functional preservation analysis*: Tab.II presents the ASR and the clean test accuracy(ACC) of the victim models concerning different backdoor attacks. Experimental results verify that our MirrorAttack achieves a

TABLE II

COMPARISON OF OUR MIRRORATTACK WITH OTHER METHODS IN TERMS OF CLEAN ACCURACY(ACC) AND ATTACK SUCCESS RATE(ASR) ON FIVE VICTIM MODELS (POINTNET, POINTNET++, DGCNN, PCT, POINTCNN) ACROSS THREE DIFFERENT DATASETS (MODELNET40, MODELNET10, SHAPENETPART). OUR METHOD ACHIEVES OUTSTANDING ASRS.

Datasets	Methods	PointNet		PointNet++		DGCNN		PCT		PointCNN	
		ACC $\uparrow$	ASR $\uparrow$	ACC $\uparrow$	ASR $\uparrow$	ACC $\uparrow$	ASR $\uparrow$	ACC $\uparrow$	ASR $\uparrow$	ACC $\uparrow$	ASR $\uparrow$
ModelNet40	PointBA-I	89.6	99.8	91.3	100	90.6	100	90.6	100	91.2	100
	PointBA-O	88.7	78.2	91.0	91.3	91.0	82.0	90.5	81.7	91.2	82.9
	IRBA	88.2	81.3	91.4	95.4	90.6	81.9	89.5	74.2	91.3	77.0
	Mirror(Ours)	89.4	82.0	91.2	99.7	91.0	99.6	90.5	98.8	91.6	99.8
ModelNet10	PointBA-I	92.5	100	92.6	100	93.5	100	93.4	100	93.3	100
	PointBA-O	91.7	79.6	92.6	95.0	93.1	86.0	93.6	86.6	93.5	84.3
	IRBA	92.9	83.1	93.5	92.8	92.4	81.6	92.8	75.9	92.3	76.9
	Mirror(Ours)	91.7	81.3	93.1	100	94.0	99.5	93.8	99.1	93.4	100
ShapeNetPart	PointBA-I	98.5	100	98.9	100	98.8	100	98.7	100	98.3	100
	PointBA-O	98.3	92.2	98.8	92.6	98.9	88.9	98.8	83.5	98.3	86.6
	IRBA	98.2	91.3	98.9	99.9	98.7	83.0	98.1	84.6	97.6	88.0
	Mirror(Ours)	98.3	94.6	98.9	99.7	98.9	99.6	98.8	99.7	98.3	100

TABLE III

BASELINE ACCURACY OF THE REPRODUCED VICTIM MODELS. ALL ATTACK METHODS IN THE TAB.II, INCLUDING OUR MIRRORATTACK, DO NOT SIGNIFICANTLY SACRIFICE ACCURACY ON BENIGN DATA

Models	ModelNet40	ModelNet10	ShapeNetPart
PointNet	88.9	92.8	98.5
PointNet++	91.4	93.7	99.0
DGCNN	91.1	94.0	98.8
PCT	90.8	93.9	98.9
PointCNN	91.4	93.3	98.4

TABLE IV

QUANTITATIVE ANALYSIS REVEALS THE IMPERCEPTIBILITY OF OUR MIRRORATTACK THROUGH MEAN ERRORS IN CHAMFER DISCREPANCY, WASSERSTEIN DISTANCE, AND HAUSDORFF DISTANCE ACROSS THREE DATASETS

Datasets	Methods	CD $\times 100\downarrow$	WD $\times 0.1\downarrow$	HD $\downarrow$
ModelNet40	PointBA-I	0.41	1.81	0.47
	PointBA-O	0.13	0.61	0.07
	IRBA	0.47	2.05	0.14
	Mirror(Ours)	0.20	0.83	0.13
ModelNet10	PointBA-I	0.33	1.83	0.43
	PointBA-O	0.12	0.50	0.06
	IRBA	0.43	2.05	0.14
	Mirror(Ours)	0.20	0.81	0.14
ShapeNetPart	PointBA-I	0.45	1.72	0.50
	PointBA-O	0.14	0.58	0.07
	IRBA	0.41	1.79	0.14
	Mirror(Ours)	0.13	0.69	0.13

marvelous ASR across all cases. Although our ASR is slightly lower than PointBA-I, we have overcome some shortcomings of PointBA-I like low imperceptibility and high vulnerability under defense measures, which will be further analyzed in V-C. We also observe that, compared to the original PointNet, our MirrorAttack demonstrates superior performance on advanced models such as PointNet++, DGCNN, PointCNN, and PCT. This suggests that these models, which place a greater emphasis on the geometric details within the point cloud, are more susceptible to vulnerabilities exploited by MirrorAttack.

To emphasize the changes in network functionality caused by the backdoor attacks, Tab.III presents the benchmark performance of the victim models. The accuracy contrast in Tab.II and Tab.III reflects that our method retains a satisfactory ACC under the premise of the high ASR. To wit, the victim model infected by MirrorAttack can still operate normally on clean samples, verifying the stealthiness of our approach.

2) *Imperceptibility analysis*: If the imperceptibility of the trigger is not limited, pursuing a high ASR becomes a competition of destruction rather than an art of balance. Therefore, the imperceptibility of the trigger is another important dimension in measuring the performance of attack algorithms. Tab.IV quantitatively measures the intensity of different backdoor triggers by computing the average deviations under multiple metrics, including the Chamfer discrepancy, Wasserstein distance, and Hausdorff distance. These three metrics each have their focuses and can comprehensively evaluate the imperceptibility. Chamfer discrepancy measures an average of the closest point distances, making it sensitive to outliers but robust against small perturbations. Hausdorff distance reflects the worst-case scenario by considering the maximum departure of the closest point. Wasserstein distance captures a notion of distribution and geometry, making it suitable for comparing two point clouds that might differ in density. Compared to the equally effective and robust IRBA, we have significantly reduced the

TABLE V

THE PENETRATIVE POWER OF DIFFERENT METHODS AGAINST SIX TYPES OF DATA AUGMENTATION AND TWO SPECIAL DEFENSE TECHNIQUES TOWARDS DGCNN ON MODELNET10. BOTH POINTBA-I AND POINTBA-O HAVE CRITICAL WEAKNESSES, WHILE IRBA AND OUR MIRRORATTACK CAN EFFECTIVELY PENETRATE VARIOUS DEFENSES

Type	Methods	PointBA-I		PointBA-O		IRBA		Mirror(Ours)	
		ACC↑	ASR↑	ACC↑	ASR↑	ACC↑	ASR↑	ACC↑	ASR↑
Augmentation	R	93.1	99.9	92.6	<b>0.0</b>	93.6	78.7	93.0	100
	R3	93.6	100	93.0	<b>0.0</b>	92.9	53.8	93.9	100
	Scaling	94.1	100	93.5	86.0	94.0	80.4	93.9	99.8
	Translation	93.1	99.6	92.4	85.5	92.3	77.8	92.9	100
	Dropout	93.3	98.5	93.5	90.6	93.8	85.9	93.2	99.3
	Jitter	93.0	100	93.1	83.2	92.4	83.0	93.2	99.6
	SOR	92.6	<b>0.0</b>	93.1	86.3	92.0	81.6	92.7	98.9
Defense	DUP	92.7	100	92.6	85.2	87.8	91.1	89.7	89.7
	LPF	92.6	99.6	92.5	80.4	93.0	77.1	93.0	88.3

TABLE VI

POINTCRT’S RECOGNITION ACCURACY FOR DIFFERENT ATTACKED SAMPLES IN MODELNET10, OUR MIRRORATTACK EXHIBITS A COMPARABLE LOW EXPOSURE RATE

	PointBA-I	PointBA-O	IRBA	Mirror(Ours)
F1↓	97.2	72.1	89.9	80.4
AUC↓	99.7	76.0	96.0	87.7

discrepancy under the Chamfer discrepancy and Wasserstein distance. Among all methods, we are only second to the rotation-based PointBA-O. This indicates that while achieving a high ASR, the MirrorAttack is still sufficiently imperceptible under various metrics.

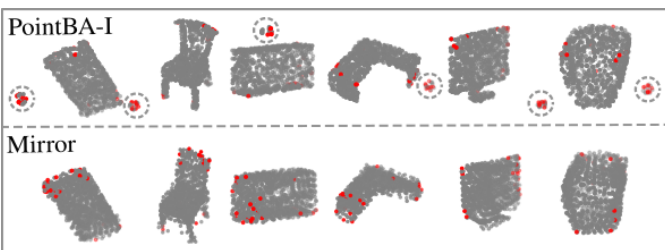


Fig. 7. Gradient-based saliency analysis with [43]. Red points are highly significant. The ball patterns(marked with dotted circles) utilized by PointBA-I are easily identifiable, whereas our MirrorAttack is challenging to locate due to its global nature.

### C. Resistance to Defense Measures

In practical applications, the collected point cloud data often contains noise, so data augmentation has become a standard technique to improve model robustness. A backdoor attack is invasive enough only if it can penetrate the commonly used data augmentation methods for the 3D point cloud. Moreover, some defense techniques are specifically designed to mitigate the invasion of attacks, which also put forward new

requirements for the effectiveness of attacks. Strictly speaking, many defense measures can also fall under the category of data augmentation. We separate the two below just for the convenience of discussion. For simplicity, we conduct all the experiments with DGCNN and ModelNet10 in this subsection.

1) *Resistance to data augmentation*: The data augmentation techniques evaluated in our study include Rotation(R), Rotation-3D (R3), Scaling, Translation, Dropout, Jitter, and Statistical Outlier Removal (SOR). Rotation involves rotating the point cloud around the  $z$ -axis by a random angle of  $10^\circ$ , whereas Rotation-3D entails rotating it around all three axes by  $10^\circ$ . Scaling and Translation are implemented following uniform distributions  $\mathcal{U}(0.95, 1.05)$  and  $\mathcal{U}([-0.05, 0.05]^3)$  respectively. Dropout technique randomly eliminates 0% to 20% of points, and Jitter introduces point-wise Gaussian noise  $\mathcal{N}(0, 0.02)$ . Statistical Outlier Removal identifies and removes outlier points based on local point density, considering a point  $p$  an outlier if the number of points within its neighborhood  $B(p, 0.1)$  is less than 50. To thoroughly assess the sensitivity of various attack algorithms to each data augmentation strategy, we initially apply them individually and subsequently in combination, as presented in Tab.V. The findings demonstrate that our method remains robust against prevalent data augmentation techniques, whereas PointBA-I shows vulnerability to SOR, and rotation-based augmentations tend to overlap PointBA-O.

2) *Resistance to expert defense techniques*: PointCRT [39] is the only existing work that specifically targets backdoor attacks on 3D point clouds. It focuses on identifying triggered point clouds within datasets using the proposed Corruption Robustness Test (CRT), which is based on the hypothesis that the classification logits of backdoor samples exhibit greater robustness to corruption. Specifically, the CRT initially evaluates the resilience of each point cloud  $x_i \in \mathcal{X}$  against 15 distinct corruption types, yielding a 15-dimensional corruption robustness feature vector  $c_i \in \mathcal{C} \subset \mathbb{R}^{15}$ . Following this, a nonlinear binary classifier  $CRT : \mathcal{C} \rightarrow \{0, 1\}$  is trained to discern whether the point cloud has been polluted by an



0	Benign	Benign	Benign	False							
1	PointBA-I	PointBA-I	$y_t$	False							
2	Mirror	Mirror	$y_t$	False							
3	Benign	PointBA-I	Benign	False							
4	PointBA-I	PointBA-I	Unrelated	False							
5	PointBA-I	PointBA-I	Benign	False							
6	PointBA-I	PointBA-I	Benign	True							
<b>Exp ID</b>	<b>Data X</b>	<b>Model f</b>	<b>Label <math>y_i</math></b>	<b>- Grad</b>	<b><math>y_t</math> = "Bed"</b>	<b>"Chair"</b>	<b>"Dresser"</b>	<b>"Desk"</b>	<b>"Monitor"</b>	<b>"Toilet"</b>	<b>Salience</b>

Fig. 8. 3D Grad-CAM for the cross-display of different point clouds  $X$ , models  $f$ , and reference labels  $y_i$ . Model "PointBA-I" means that it has been hijacked with the PointBA-I attack. "-Grad" indicates whether we inverse the gradient (True) for counterfactual study or not (False). Exp.0-Exp.2 once again confirm the difficulty of locating the mirror trigger. Exp.3 demonstrate that the hijack diminishes the model's ability to display salient areas of benign data. The blue box reveals a competitive relationship between the trigger box and the source feature. The high consistency of the two yellow boxes mutually validates this competitive relationship. For a detailed analysis, please refer to main text V-C4.

attack. Two classic binary classification metrics, F1 score(F1) and Area Under Curve(AUC), are used to assess whether PointCRT can identify the corresponding triggered point cloud, with lower scores indicating stronger penetration of the attack. Tab.VI shows the detection effectiveness of PointCRT against different attack methods, among which MirrorAttack demonstrates penetration strength second only to PointBA-O.

Considering that current backdoor defense methods for 3D point clouds are very limited, we additionally introduce two adversarial defense algorithms oriented toward 3D point clouds in Tab.V. [40] observed that the attack pattern typically resides in the high-frequency portion of the spherical harmonic domain and consequently designed a low-pass filter (LPF) to eliminate the attack. [41] proposed a denoise and upsampling(DUP) method to tackle the attack. Experimental results indicate that our MirrorAttack can also resist these two different types of adversarial defense algorithms.

3) *Resistance to gradient-based salience detection*: Some points are regarded as *salient points* when the perturbation on them significantly influences the model's decision-making. The appearance of the trigger pattern can markedly impact the result of classification. Thus, it is practical to explore revealing some trigger patterns by detecting these salient points. We apply a gradient-based salience detection method proposed in [43]. Given a point cloud  $X$ , [43] transforms  $X$  to a spherical coordinate system and perturbs it by moving a point  $x_i \in X$  towards the center  $c = \text{median}(X)$ . We have:

$$\frac{\partial \mathcal{L}}{\partial r_i} = \frac{\partial \mathcal{L}}{\partial x_i} \cdot \frac{x_i - c}{r_i}. \quad (28)$$

If reducing  $r_i$  results in an increase in  $\mathcal{L}$ , it indicates that  $x_i$  positively contributes to the correct inference. Define  $\rho_i = r_i^{-\alpha}$  ( $\alpha > 0$  is a scaling factor). Since  $\rho_i$  and  $r_i$  are inversely proportional, the  $\partial \mathcal{L} / \partial \rho_i$  can be directly defined as the significance value  $s_i$ :

$$s_i = \frac{\partial \mathcal{L}}{\partial \rho_i} \propto - \frac{\partial \mathcal{L}}{\partial r_i} r_i^{1+\alpha}. \quad (29)$$

We choose a standard  $\alpha = 1$  and compares our method with PointBA-I in Fig.7. The top 2% of points with the highest significance are marked in red. As expected, the ball pattern of PointBA-I is well exposed, whereas the trigger pattern of MirrorAttack, being dispersed globally, is difficult to locate. Similar results are also presented in [35].

4) *Traits Under 3D Grad-CAM*: The Gradient Class Activation Map(Grad-CAM) [42] also utilizes a model's gradients to spotlight critical image areas for class identification, offering visual insights into the model's decision-making process and enhancing our understanding of its behavior. Unlike the previous section where [43] considers the relationship between *point* perturbation and *loss*, Grad-CAM delivers a more fine-grained analysis on the relationship between *feature* perturbation and the confidence of a specific *class*. Therefore, Grad-CAM can more profoundly reveal the backdoor pattern and the characteristics of the hijacked model.

We implement the Grad-CAM for 3D point clouds in the following way: Assume that the point cloud  $X \in \mathbb{R}^{N \times 3}$  is encoded by a DGCNN backbone, resulting in a point-wise feature  $A_X \in \mathbb{R}^{N \times c}$ , and a subsequent classifier  $cls : A_X \mapsto \hat{y}$

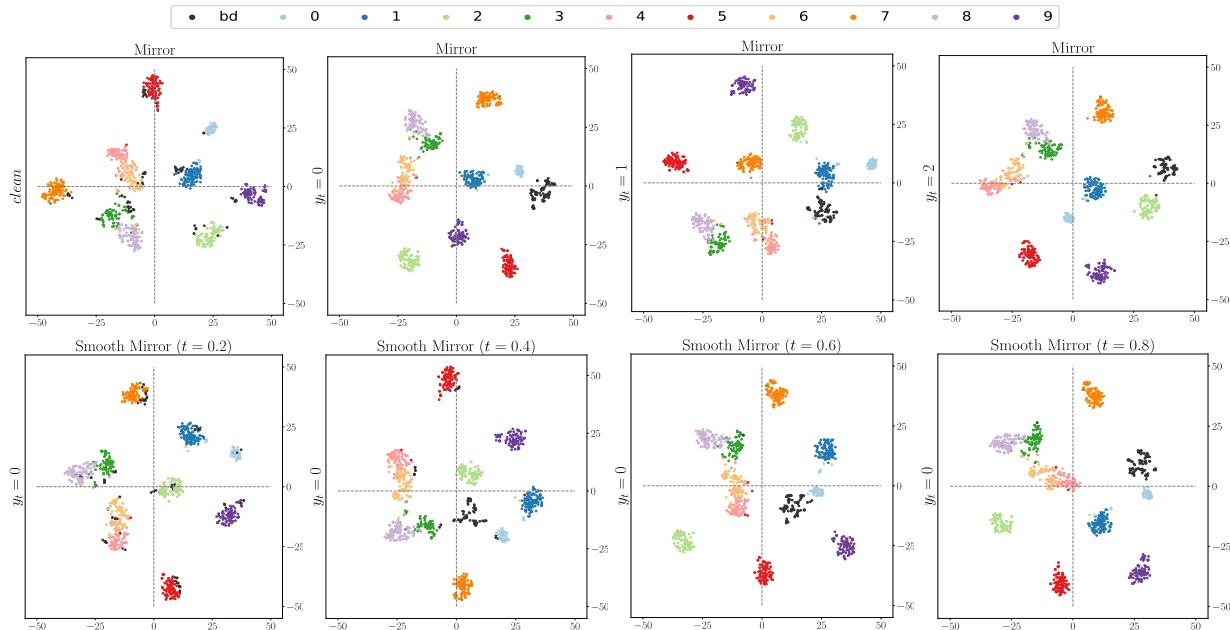


Fig. 9. DGCNN’s feature visualization on ModelNet10 with t-SNE dimensionality reduction [61]. The first row shows that different target labels induce mirror sample features to approach and cluster around the corresponding samples. The second row demonstrates the performance of trigger smoothing in the feature space, with features increasingly deviating and clustering as the attack intensity increases. The attacked samples are randomly chosen from all classes.

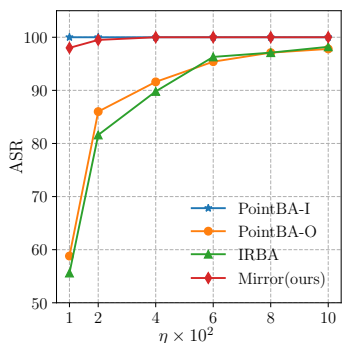


Fig. 10. Effect of the poison rate  $\eta$  towards DGCNN on ModelNet10. Our method maintains a high ASR even at very low poisoning rates(1%), while the ASRs of PointBA-O and IRBA significantly decrease.

TABLE VII  
EFFECT OF TARGET LABEL.

Datasets	$y_t = 0$		$y_t = 1$		$y_t = 2$	
	ACC $\uparrow$	ASR $\uparrow$	ACC $\uparrow$	ASR $\uparrow$	ACC $\uparrow$	ASR $\uparrow$
ModelNet40	90.4	99.4	90.7	99.5	90.5	99.5
ModelNet10	93.2	99.5	93.3	100	93.3	99.8
ShapeNetPart	98.7	99.8	98.7	99.1	98.9	99.8

maps these features to a soft class distribution. Here,

$$w_{j,k}^i = \frac{\partial \hat{y}_i}{\partial A_{X,j,k}}, \quad w_k^i = \sum_j w_{j,k}^i, \quad (30)$$

represent the response level of each spatial location  $j$  and channel  $k$  within the feature  $A_X$  towards the  $i$ -th class respectively. We obtain channel-wise attention  $w_k^i \in \mathbb{R}^c$  by summing across the spatial dimension and utilize it to reweight

the feature map  $A_X$ . Then, a ReLU is attached to retain those channels that have a positive response to the  $i$ -th class and finally we have the saliency map  $X_s^i \in \mathbb{R}^N$ :

$$X_s^i = \text{ReLU}\left(\sum_k w_k^i A_{X,:,k}\right). \quad (31)$$

where  $A_{X,:,k}$  denotes the slice of  $A_X$  along channel  $k$ .

Multiple experiments are conducted involving various data  $X$ , models  $f$ , and reference labels  $y_i$  in Fig.8. For instance, Exp.3 utilizes a benign model to identify PointBA-I data and derived partial derivatives for each sample’s initial category. Exp.0 serves as a blank control group, reflecting normal significant areas. Exp.1 demonstrates that the ball pattern is easily recognized by the 3D Grad-CAM, whereas Exp.2 shows that the Mirror trigger is difficult to locate due to its dispersed pattern, consistent with the conclusions in Fig.7. Changing the model to one hijacked by PointBA-I in Exp.3 results in the inability to normally display significant areas. Exp.4 reveals that the trigger is only exposed when we take the partial derivative of the target class  $y_t$ . In Exp.5, the bed’s original category and the target label overlapped, and the 3D Grad-CAM fully highlights the trigger while ignoring the aboriginal patterns, indicating that the trigger is a very strong feature, consistent with the hypothesis in [25].

We also conduct a counterfactual study in Exp.6 by inverting the gradients:

$$X_{-s}^i = \text{ReLU}\left(-\sum_k w_k^i A_{X,:,k}\right). \quad (32)$$

In contrary to the saliency map  $X_s^i$  which reveals areas positively correlated with class  $i$ ,  $X_{-s}^i$  shows the region that will reduce the confidence of the target class and compete with the  $X_s^i$ . For example, in [42], when both a cat and

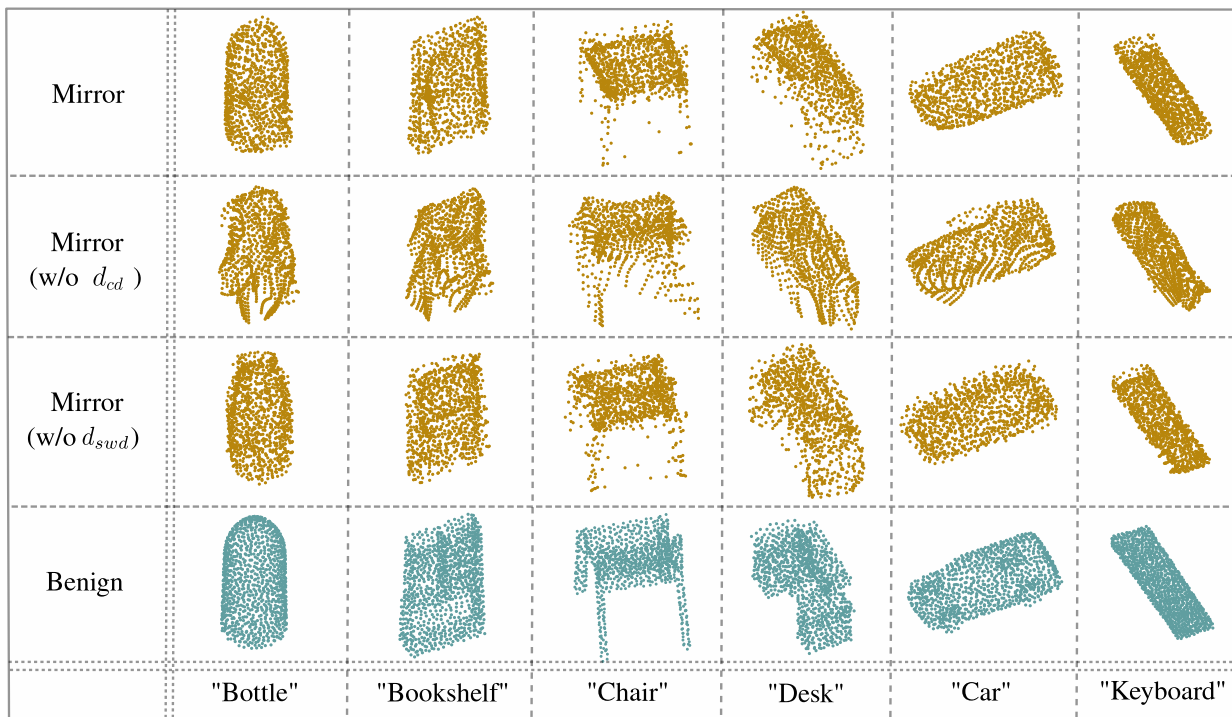


Fig. 11. Visualizations of attack samples generated by auto-encoders trained under different metrics. The reconstruction is poor constrained only by  $d_{SWD}$ , losing the imperceptible of the trigger.

a dog appear in one image, taking the partial derivative of "dog", then  $X_s^i$  highlights the dog while  $X_{-s}^i$  highlights the cat. In our task, the trigger pattern and the original feature pattern of the sample also form a *competitive* relationship. For target class  $y_t = \text{"bed"}$ ,  $X_{-s}^i$  exhibit a reverse form of  $X_s^i$  in Exp.5, indicating that  $X_{-s}^i$  is able to release the original characteristics suppressed by the trigger pattern (blue box in Fig.8). For other non-target classes, the highlighted regions almost coincide with those activated by the target class  $y_t$  shown in Exp.1 (yellow boxes in Fig.8), which completely aligns with our reasoning about the competitive region.

The 3D Grad-CAM also helps us understand the impact of the target label selected on backdoor attack performance, which we will discuss in Sec.V-D2 below.

#### D. Ablation Studies

1) *Effect of poisoning rate*: The poisoning rate  $\eta$  determines the trade-off between attack concealment and effectiveness. The ideal attack algorithm should achieve a high ASR with a small  $\eta$ . We explore the trend of ASR with increasing  $\eta$  on different methods in Fig.10. The results show that our transformation-based MirrorAttack still maintains a high ASR even at a very low  $\eta$ , benchmarking against interaction-based methods, while other transformation-based methods experience a significant decrease in ASR at low poisoning rates.

2) *Effect of target category*: We and our pioneer studies on backdoor attacks [32] [34] choose a minority of target classes as representatives to save on experimental expenses. One may wonder whether the target category  $y_t$  we choose is representative. [34] provides empirical experimental results and speculated that the target label has little impact on IRBA.

However, the principle behind this phenomenon remains elusive.

To remedy this gap, we combine the latest theoretical research [25], as well as experiments from multiple perspectives in Tab.VII, Fig.9, and Fig.8, to further discuss the impact of the target label on backdoor attacks. Tab.VII presents the performance of our method when attacking other target categories, with the victim model being DGCNN. Switching target categories does not significantly affect the backdoor attack performance.

Some works might help us understand this phenomenon. Classical backdoor defense literature [24] suggests that the essence of backdoor attacks lies in establishing shortcuts between backdoor samples and any arbitrary target category in the victim network. Namely, the trigger pattern bypasses the pathway of the source image in the inference graph, activating a shorter, alternative pathway. Meanwhile, [25] assumes that the trigger often acts as the *strongest* feature, suppressing the natural characteristics (usually reflected in the original label) of the source images. Removing the strongest feature leads to significant defensive performance. The 3D Grad-CAM we implemented reveals that the trigger pattern has gained overwhelming advantage in the competition with the aboriginal patterns (reflected in the blue and yellow boxes in Fig.8), which corroborates the assumptions of [24] and [25].

Extensive qualitative experiments in Fig.9 visualizes the feature space of the ModelNet10 test set by reducing dimensions using t-SNE [61]. Regardless of the class of the source samples, mirror samples always manage to distance themselves from the source samples and form a new cluster near the indigenous samples. Of course, separability in feature

TABLE VIII  
TRIGGER IMPERCEPTIBILITY UNDER DIFFERENT SETTINGS. THE SYNERGISTIC EFFECT OF TWO LOSSES GENERATES THE MOST IMPERCEPTIBLE TRIGGER

Methods	CD $\times 100 \downarrow$	WD $\times 0.1 \downarrow$	HD $\downarrow$
Mirror	0.20	0.81	0.14
Mirror(w/o $d_{SWD}$ )	0.21	1.41	0.13
Mirror(w/o $d_{CD}$ )	0.32	0.83	0.16

TABLE IX  
TRIGGER EFFECTIVENESS UNDER DIFFERENT SETTINGS

Methods	PointNet		PointNet++		DGCNN	
	ACC $\uparrow$	ASR $\uparrow$	ACC $\uparrow$	ASR $\uparrow$	ACC $\uparrow$	ASR $\uparrow$
Mirror	91.7	81.3	93.1	100	94.0	99.5
Mirror(w/o $d_{SWD}$ )	92.0	72.6	92.5	98.6	93.1	99.3
Mirror(w/o $d_{CD}$ )	91.9	98.0	93.8	100	93.8	100

space is not a necessary condition for a successful attack [25] [31]. We find that the feature distribution of a low-intensity ( $t \leq 0.2$ ) MirrorAttack is similar to the benign situation. However, it still achieves a considerable ASR (see in Fig.12b, Sec.V-D4), devoid of the feature separability. It is foreseeable that low-intensity MirrorAttack will be able to resist future point cloud backdoor defense methods based on the feature separation assumption.

3) *Effect of trigger configuration*: Below, we discuss the impact of different mirror training configurations on the triggers produced, including aspects of stealth and effectiveness. Tab.VIII presents the stealth of mirror triggers on ModelNet10 when trained with different loss functions. The synergy between  $d_{CD}$  and  $d_{SWD}$  makes the final version of the mirror very stealthy across three metrics. The absence of either  $d_{CD}$  or  $d_{SWD}$  leads to more conspicuous triggers under the respective metrics, with little difference under the Hausdorff metric. Tab.IX, on the other hand, measures the effectiveness of different mirror triggers from the perspective of attack success. It is observable that mirror triggers under different configurations can effectively attack, with only the  $d_{SWD}$  constraint achieving a good ASR. However, as shown in the visual results in Fig.11, the mirror trigger under only the  $d_{SWD}$  constraint has poor reconstruction quality, sacrificing stealth.

4) *Effect of smoothing configuration*: The trigger smoothing module based on spherical harmonic transformations has two crucial parameters: the attack intensity  $t$  and the maximum degree of transformation  $N_l$ . We demonstrate their impact on the stealth of smoothed triggers on ModelNet10 in Fig.12a. On one hand, we find that under the standard of Chamfer discrepancy, as  $t$  increases, the backdoor point clouds smoothly transition from benign samples to mirror samples. On the other hand, with  $t = 0$ , as  $N_l$  gradually increases to 100, the error caused by the truncation of spherical harmonic tail terms nearly drops to zero, indicating that  $N_l = 100$  is sufficient for the reconstruction. Fig.12b then shows the impact of attack intensity  $t$  on the ASR. We find that both PointNet++

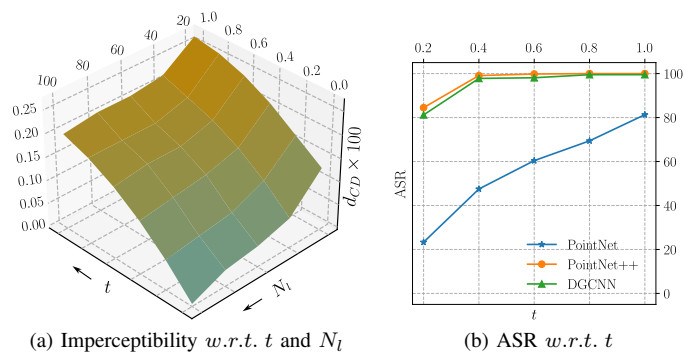


Fig. 12. The impact of trigger smoothing parameters on the imperceptibility and ASR. (a) Initially, at  $t = 0$ , the curve shows the influence of the spherical harmonics expansion order  $N_l$  on the reconstruction error, which becomes negligible when  $N_l = 100$ . Subsequently, with  $N_l = 100$ , the curve demonstrates that as the attack intensity  $t$  increases, the mean Chamfer error also smoothly rises and the ASRs on three different models also increases (b).

and DGCNN are extremely sensitive to the MirrorAttack, achieving nearly 100 ASR even at  $t = 0.4$ . This once again confirms the significance of trigger smoothing: under the premise of ensuring a nearly 100 ASR on PointNet++ and DGCNN, the imperceptibility of the trigger is significantly enhanced.

## VI. LIMITATIONS AND FUTURE WORK

### A. Extending application scenarios

Mirror trigger, although very good in terms of metrics, is somewhat lacking in the depiction of details such as the legs of chairs and tables. With the work on 3D point cloud reconstruction already mature, making triggers more concealed has become relatively easy. However, whether it can still maintain a satisfactory ASR remains to be further studied. Additionally, unlike triggers such as interaction and rotation that can be directly transferred to any scene, MirrorAttack requires adjusting the reconstruction network according to the nature of the victim dataset to rebalance concealment and effectiveness. In the future, we will transfer MirrorAttack to more complex scenarios [50] [51] [52] [53].

### B. Delving into the principles

We found that MirrorAttack can easily attack networks with the ability to depict local geometric details such as PointNet++, DGCNN, PCT, and PointCNN, but it is not prominent on PointNet. Currently, in the image domain, [30] has found that multi-head attention modules are sensitive to backdoor attacks, while there is still little research on what structures in 3D point cloud networks are more sensitive to backdoor attacks. In the future, we will explore the principles behind the sensitivity differences of point cloud networks to different triggers. This will not only help MirrorAttack further conquer PointNet but more importantly, it will inspire researchers of point cloud networks to design more robust models.

### C. Improving the trigger smoothing method

The core challenge of Trigger Smoothing lies in the correspondence between clean point clouds and triggered point



clouds. Although we have achieved the homotopy of the latent surface with the help of spherical harmonic transformation, it essentially further shifts the difficulty to the correspondence of point cloud sampling locations. In triggers based on reconstruction like MirrorAttack, since the relative position between clean point clouds and triggered point clouds is relatively fixed, we can assume there is no significant difference in the distribution of the point clouds. However, once this premise is broken, such as when involving rotation, the current module is no longer applicable. Future improvements can be made from two aspects: further optimizing the trigger smoothing module, and requiring smoothness from the design inception of the trigger.

Never forget that the research on backdoor attacks is not for destruction but to promote stronger defense algorithms and more robust models.

## VII. CONCLUSION

This paper addresses the requirements for backdoor attacks and highlights the existing gaps in 3D point cloud backdoor attack methodologies. Drawing inspiration from advancements in the image domain, we introduce MirrorAttack, a novel strategy formulated through the 3D point cloud reconstruction network. Characterized by its simplicity, efficacy, imperceptibility, and resilience, MirrorAttack represents a noteworthy advancement in this area of research. Furthermore, the incorporation of a trigger smoothing module, leveraging spherical harmonic transformation, enhances MirrorAttack's adaptability, offering a new approach to trigger manipulation. Through extensive quantitative and qualitative assessments, we have validated MirrorAttack's potency. We also conclude our work with a critical examination of MirrorAttack's limitations, proposing avenues for refinement and urging further research to fortify the robustness of models against backdoor threats.

## ACKNOWLEDGMENTS

This research is sponsored by the National Natural Science Foundation of China (NSFC, Grant No. 62272082 and No. 62301562), and the China Postdoctoral Science Foundation (Grant No. 2023M733756).

We thank Mr. Gao from Shenzhen International Graduate School, Tsinghua University for inspiring and assisting us with some of the problems encountered during our research. We also express our gratitude to all the authors of the open-source projects used in this study for generously sharing their work.

The responsibility for the content and any remaining errors is exclusively with the authors.

## REFERENCES

- [1] Qi, C., Su, H., Mo, K. & Guibas, L. Pointnet: Deep learning on point sets for 3d classification and segmentation. *Proceedings Of The IEEE Conference On Computer Vision And Pattern Recognition*. pp. 652-660 (2017)
- [2] Qi, C., Yi, L., Su, H. & Guibas, L. Pointnet++: Deep hierarchical feature learning on point sets in a metric space. *Advances In Neural Information Processing Systems*. **30** (2017)
- [3] Ma, X., Qin, C., You, H., Ran, H. & Fu, Y. Rethinking network design and local geometry in point cloud: A simple residual MLP framework. *ArXiv Preprint arXiv:2202.07123*. (2022)
- [4] Li, Y., Bu, R., Sun, M., Wu, W., Di, X. & Chen, B. Pointcnn: Convolution on x-transformed points. *Advances In Neural Information Processing Systems*. **31** (2018)
- [5] Wu, W., Qi, Z. & Fuxin, L. Pointconv: Deep convolutional networks on 3d point clouds. *Proceedings Of The IEEE/CVF Conference On Computer Vision And Pattern Recognition*. pp. 9621-9630 (2019)
- [6] Thomas, H., Qi, C., Deschaud, J., Marcotegui, B., Goulette, F. & Guibas, L. Kpconv: Flexible and deformable convolution for point clouds. *Proceedings Of The IEEE/CVF International Conference On Computer Vision*. pp. 6411-6420 (2019)
- [7] Wang, Y., Sun, Y., Liu, Z., Sarma, S., Bronstein, M. & Solomon, J. Dynamic graph cnn for learning on point clouds. *ACM Transactions On Graphics (tog)*. **38**, 1-12 (2019)
- [8] Shi, W. & Rajkumar, R. Point-gnn: Graph neural network for 3d object detection in a point cloud. *Proceedings Of The IEEE/CVF Conference On Computer Vision And Pattern Recognition*. pp. 1711-1719 (2020)
- [9] Vaswani, A., Shazeer, N., Parmar, N., Uszkoreit, J., Jones, L., Gomez, A., Kaiser, Ł. & Polosukhin, I. Attention is all you need. *Advances In Neural Information Processing Systems*. **30** (2017)
- [10] Guo, M., Cai, J., Liu, Z., Mu, T., Martin, R. & Hu, S. Pct: Point cloud transformer. *Computational Visual Media*. **7** pp. 187-199 (2021)
- [11] Zhao, H., Jiang, L., Jia, J., Torr, P. & Koltun, V. Point transformer. *Proceedings Of The IEEE/CVF International Conference On Computer Vision*. pp. 16259-16268 (2021)
- [12] Tian, S., Liu, J. & Liu, X. Towards class-agnostic tracking using feature decorrelation in point clouds. *IEEE Transactions On Image Processing*. (2024)
- [13] Li, Y., Ma, L., Zhong, Z., Liu, F., Chapman, M., Cao, D. & Li, J. Deep learning for lidar point clouds in autonomous driving: A review. *IEEE Transactions On Neural Networks And Learning Systems*. **32**, 3412-3432 (2020)
- [14] Yu, J., Zhang, C., Wang, H., Zhang, D., Song, Y., Xiang, T., Liu, D. & Cai, W. 3d medical point transformer: Introducing convolution to attention networks for medical point cloud analysis. *ArXiv Preprint arXiv:2112.04863*. (2021)
- [15] Liu, Y., Li, W., Liu, J., Chen, H. & Yuan, Y. GRAB-Net: Graph-based boundary-aware network for medical point cloud segmentation. *IEEE Transactions On Medical Imaging*. (2023)
- [16] Blanc, T., El Beheiry, M., Caporal, C., Masson, J. & Hajj, B. Genuage: visualize and analyze multidimensional single-molecule point cloud data in virtual reality. *Nature Methods*. **17**, 1100-1102 (2020)
- [17] Kästner, L., Frasineanu, V. & Lambrecht, J. A 3d-deep-learning-based augmented reality calibration method for robotic environments using depth sensor data. *2020 IEEE International Conference On Robotics And Automation (ICRA)*. pp. 1135-1141 (2020)
- [18] Gu, T., Liu, K., Dolan-Gavitt, B. & Garg, S. Badnets: Evaluating backdooring attacks on deep neural networks. *IEEE Access*. **7** pp. 47230-47244 (2019)
- [19] Chen, X., Liu, C., Li, B., Lu, K. & Song, D. Targeted backdoor attacks on deep learning systems using data poisoning. *ArXiv Preprint arXiv:1712.05526*. (2017)
- [20] Zeng, Y., Park, W., Mao, Z. & Jia, R. Rethinking the backdoor attacks' triggers: A frequency perspective. *Proceedings Of The IEEE/CVF International Conference On Computer Vision*. pp. 16473-16481 (2021)
- [21] Nguyen, A. & Tran, A. Wanet-imperceptible warping-based backdoor attack. *ArXiv Preprint arXiv:2102.10369*. (2021)
- [22] Nguyen, T. & Tran, A. Input-aware dynamic backdoor attack. *Advances In Neural Information Processing Systems*. **33** pp. 3454-3464 (2020)
- [23] Li, Y., Li, Y., Wu, B., Li, L., He, R. & Lyu, S. Invisible backdoor attack with sample-specific triggers. *Proceedings Of The IEEE/CVF International Conference On Computer Vision*. pp. 16463-16472 (2021)
- [24] Wang, B., Yao, Y., Shan, S., Li, H., Viswanath, B., Zheng, H. & Zhao, B. Neural cleanse: Identifying and mitigating backdoor attacks in neural networks. *2019 IEEE Symposium On Security And Privacy (SP)*. pp. 707-723 (2019)
- [25] Khaddaj, A., Leclerc, G., Makelov, A., Georgiev, K., Salman, H., Ilyas, A. & Madry, A. Rethinking Backdoor Attacks. (2023)
- [26] Huang, K., Li, Y., Wu, B., Qin, Z. & Ren, K. Backdoor defense via decoupling the training process. *ArXiv Preprint arXiv:2202.03423*. (2022)
- [27] Liu, Y., Fan, M., Chen, C., Liu, X., Ma, Z., Wang, L. & Ma, J. Backdoor defense with machine unlearning. *IEEE INFOCOM 2022-IEEE Conference On Computer Communications*. pp. 280-289 (2022)
- [28] Li, Y., Jiang, Y., Li, Z. & Xia, S. Backdoor learning: A survey. *IEEE Transactions On Neural Networks And Learning Systems*. (2022)
- [29] Gao, Y., Doan, B., Zhang, Z., Ma, S., Zhang, J., Fu, A., Nepal, S. & Kim, H. Backdoor attacks and countermeasures on deep learning: A comprehensive review. *ArXiv Preprint arXiv:2007.10760*. (2020)



- [30] Yuan, Z., Zhou, P., Zou, K. & Cheng, Y. You Are Catching My Attention: Are Vision Transformers Bad Learners Under Backdoor Attacks?. *Proceedings Of The IEEE/CVF Conference On Computer Vision And Pattern Recognition*. pp. 24605-24615 (2023)
- [31] Mo, X., Zhang, Y., Zhang, L., Luo, W., Sun, N., Hu, S., Gao, S. & Xiang, Y. Robust Backdoor Detection for Deep Learning via Topological Evolution Dynamics. *2024 IEEE Symposium On Security And Privacy (SP)*. pp. 171-171 (2024)
- [32] Li, X., Chen, Z., Zhao, Y., Tong, Z., Zhao, Y., Lim, A. & Zhou, J. Pointba: Towards backdoor attacks in 3d point cloud. *Proceedings Of The IEEE/CVF International Conference On Computer Vision*. pp. 16492-16501 (2021)
- [33] Xiang, Z., Miller, D., Chen, S., Li, X. & Kesidis, G. A backdoor attack against 3d point cloud classifiers. *Proceedings Of The IEEE/CVF International Conference On Computer Vision*. pp. 7597-7607 (2021)
- [34] Gao, K., Bai, J., Wu, B., Ya, M. & Xia, S. Imperceptible and robust backdoor attack in 3d point cloud. *IEEE Transactions On Information Forensics And Security*. **19** pp. 1267-1282 (2023)
- [35] Fan, L., He, F., Si, T., Fan, R., Ye, C. & Li, B. MBA: Backdoor Attacks against 3D Mesh Classifier. *IEEE Transactions On Information Forensics And Security*. (2023)
- [36] Fan, L., He, F., Guo, Q., Tang, W., Hong, X. & Li, B. Be Careful with Rotation: A Uniform Backdoor Pattern for 3D Shape. *ArXiv Preprint arXiv:2211.16192*. (2022)
- [37] Tian, G., Jiang, W., Liu, W. & Mu, Y. Poisoning morphnet for clean-label backdoor attack to point clouds. *ArXiv Preprint arXiv:2105.04839*. (2021)
- [38] Feng, L., Qian, Z., Zhang, X. & Li, S. Stealthy Backdoor Attacks On Deep Point Cloud Recognition Networks. *The Computer Journal*. pp. bxad109 (2023)
- [39] Hu, S., Liu, W., Li, M., Zhang, Y., Liu, X., Wang, X., Zhang, L. & Hou, J. Pointcrt: Detecting backdoor in 3d point cloud via corruption robustness. *Proceedings Of The 31st ACM International Conference On Multimedia*. pp. 666-675 (2023)
- [40] Naderi, H., Noorbakhsh, K., Etemadi, A. & Kasaei, S. LPF-Defense: 3D adversarial defense based on frequency analysis. *Plos One*. **18**, e0271388 (2023)
- [41] Zhou, H., Chen, K., Zhang, W., Fang, H., Zhou, W. & Yu, N. Dup-net: Denoiser and upsampler network for 3d adversarial point clouds defense. *Proceedings Of The IEEE/CVF International Conference On Computer Vision*. pp. 1961-1970 (2019)
- [42] Selvaraju, R., Cogswell, M., Das, A., Vedantam, R., Parikh, D. & Batra, D. Grad-cam: Visual explanations from deep networks via gradient-based localization. *Proceedings Of The IEEE International Conference On Computer Vision*. pp. 618-626 (2017)
- [43] Zheng, T., Chen, C., Yuan, J., Li, B. & Ren, K. Pointcloud saliency maps. *Proceedings Of The IEEE/CVF International Conference On Computer Vision*. pp. 1598-1606 (2019)
- [44] Balta, H., Velagic, J., Bosschaerts, W., De Cubber, G. & Siciliano, B. Fast statistical outlier removal based method for large 3D point clouds of outdoor environments. *IFAC-PapersOnLine*. **51**, 348-353 (2018)
- [45] Nguyen, T., Pham, Q., Le, T., Pham, T., Ho, N. & Hua, B. Point-set distances for learning representations of 3d point clouds. *Proceedings Of The IEEE/CVF International Conference On Computer Vision*. pp. 10478-10487 (2021)
- [46] Barrow, H., Tenenbaum, J., Bolles, R. & Wolf, H. Parametric correspondence and chamfer matching: Two new techniques for image matching. *Proceedings: Image Understanding Workshop*. pp. 21-27 (1977)
- [47] Vaserstein, L. Markov processes over denumerable products of spaces, describing large systems of automata. *Problemy Peredachi Informatsii*. **5**, 64-72 (1969)
- [48] Kolouri, S., Nadjahi, K., Simsekli, U., Badeau, R. & Rohde, G. Generalized sliced wasserstein distances. *Advances In Neural Information Processing Systems*. **32** (2019)
- [49] Huttenlocher, D., Klanderman, G. & Rucklidge, W. Comparing images using the Hausdorff distance. *IEEE Transactions On Pattern Analysis And Machine Intelligence*. **15**, 850-863 (1993)
- [50] Geiger, A., Lenz, P. & Urtasun, R. Are we ready for autonomous driving? the kitti vision benchmark suite. *2012 IEEE Conference On Computer Vision And Pattern Recognition*. pp. 3354-3361 (2012)
- [51] Hackel, T., Savinov, N., Ladicky, L., Wegner, J., Schindler, K. & Pollefeys, M. Semantic3d. net: A new large-scale point cloud classification benchmark. *ArXiv Preprint arXiv:1704.03847*. (2017)
- [52] Caesar, H., Bankiti, V., Lang, A., Vora, S., Liong, V., Xu, Q., Krishnan, A., Pan, Y., Baldan, G. & Beijbom, O. nuscenes: A multimodal dataset for autonomous driving. *Proceedings Of The IEEE/CVF Conference On Computer Vision And Pattern Recognition*. pp. 11621-11631 (2020)
- [53] Sun, P., Kretzschmar, H., Dotiwalla, X., Chouard, A., Patnaik, V., Tsui, P., Guo, J., Zhou, Y., Chai, Y., Caine, B. & Others Scalability in perception for autonomous driving: Waymo open dataset. *Proceedings Of The IEEE/CVF Conference On Computer Vision And Pattern Recognition*. pp. 2446-2454 (2020)
- [54] Kingma, D. & Ba, J. Adam: A method for stochastic optimization. *ArXiv Preprint arXiv:1412.6980*. (2014)
- [55] Yang, Y., Feng, C., Shen, Y. & Tian, D. Foldingnet: Point cloud auto-encoder via deep grid deformation. *Proceedings Of The IEEE Conference On Computer Vision And Pattern Recognition*. pp. 206-215 (2018)
- [56] Yang, G., Huang, X., Hao, Z., Liu, M., Belongie, S. & Hariharan, B. Pointflow: 3d point cloud generation with continuous normalizing flows. *Proceedings Of The IEEE/CVF International Conference On Computer Vision*. pp. 4541-4550 (2019)
- [57] Luo, S. & Hu, W. Diffusion probabilistic models for 3d point cloud generation. *Proceedings Of The IEEE/CVF Conference On Computer Vision And Pattern Recognition*. pp. 2837-2845 (2021)
- [58] Agarap, A. Deep learning using rectified linear units (relu). *ArXiv Preprint arXiv:1803.08375*. (2018)
- [59] Ioffe, S. & Szegedy, C. Batch normalization: Accelerating deep network training by reducing internal covariate shift. *International Conference On Machine Learning*. pp. 448-456 (2015)
- [60] Wiecek, M. & Meschede, M. SHTools: Tools for working with spherical harmonics. *Geochemistry, Geophysics, Geosystems*. **19**, 2574-2592 (2018)
- [61] Maaten, L. & Hinton, G. Visualizing data using t-SNE. *Journal Of Machine Learning Research*. **9** (2008)